ISSN 0915-633

NATIONAL INSTITUTE FOR FUSION SCIENCE

Characteristics for Metal Plate Penetration of a Low Energy Negative Muonlike or Pionlike Particle Beam

J. Uramoto

(Received - Mar. 22, 1995)

NIFS-350 Apr. 1995

RESEARCH REPORT
NIFS Series

NAGOYA, JAPAN

Characteristics for Metal Plate Penetration of a Low Energy Negative Muonlike or Pionlike Particle Beam

Jōshin URAMOTO

National Institute for Fusion Science

Nagoya 464-01, Japan

Abstract

It is proved experimentally that a low energy (< 1000 eV) negative muonlike or pionlike particle beam produced by an electron bunch and a positive ion bunch, penetrates through a metal plate of about 1 cm in thickness without energy loss. As a necessary condition, some positive ions are supplied in the vacuum region after penetration of the metal plate.

Keywords: negative muonlike particle μ^-, negative pionlike particle π^-, metal plate penetration, positive ion

1. Introduction

We have already reported[1] the following experimental facts: When a low energy electron beam ($\leq$ 1200 eV) is injected perpendicularly to a uniform magnetic field, together with a low energy positive ion beam which is stopped electrically and the uniform magnetic field is used as a mass analyzer, two peak of negative current to the beam collector appear at two analyzing magnetic field intensities which correspond to two relations of negative muon (the mass $m_1 = 207\ m_e$ and the charge $q_1 = e$) and negative pion (the mass $m_2 = 273\ m_e$ and the charge $q_2 = e$, where m_e and e are mass and charge of electron). In this new report, some remarkable characteristics of metal plate penetration for the negative muonlike particle μ^- and pionlike particle π^- beam, will be investigated experimentally in order to classify them from usual electron and negative ion beams.

2. Basic Experimental Conditions

Schematic diagrams of the basic experimental apparatus are shown in Fig. 1 and Fig. 2. The initial or first electron beam (F.E.B.) is stopped critically in front of the entrance slit S by an electrical potential of the decelerator D connected to the cathode of the electron gun. Next, a neutral gas is introduced into the first electron beam region and a plasma is produced through ionization of the gas. Then, positive ions of the plasma are accelerated in front of S while a positive ion beam with an energy corresponding to the first electron beam acceleration voltage V_A, is injected into the magnetic field region through S. Moreover, the stopped beam electrons are reaccelerated electrically toward the gap between two magnetic poles (N) and (S) through S, while the injected ion beam is decelerated electrically and stopped in the gap. The electrically reaccelerated electrons are injected perpendicularly to the magnetic field (B_M) and bunched in cyclotron motions of small radius.

As shown in Fig. 2, the above magnetic system is used as a mass analyzer (M.A.) of 90° type when the beam collector B.C. is arranged. The analyzing curvature radius r is 4.3 cm. It should be noted that the bias voltage V_S of the beam collector is positive with respect to the mass analyzer in order to measure a negative charge current.

A fringe magnetic field distribution of the analyzing magnetic field B_M under a magnetic coil current of 1A, is shown in Fig. 3 for two different metal plates as the entrance plate (decelerator

D) of Fig. 1 and Fig. 2. The iron (Fe) plate is used and the fringe magnetic field is much reduced.

The distribution of electrically applied potential are shown in Fig. 4. The first electron beam from the electron gun is perfectly reflected in front of the entrance slit S of the magnetic mass analyzer (M.A.) while a plasma is produced by a gas (air) ionization. Then, a positive ion beam is injected into M.A. through the slit S and the second electron beam is produced by reacceleration of the plasma electrons. It should be noted that the injected positive ion beam (i_2) is decelerated and stopped electrically, and that the second electron beam (e_2) suffers a magnetron (cyclotron) motion in the uniform magnetic field (which is used as the analyzing magnetic field of M.A.). As a result, both the electron beam and positive ion beam will be bunched within the small space at the entrance X of the uniform magnetic field. As reported already,[1] we consider that a negative muonlike μ^- and a negative pionlike π^- particle beams are produced by a coherent interaction between the bunched electrons and positive ions. Because we find that the mass analyzing relations of negative muon and negative pion are satisfied for two peaks of negative current I^- to the beam collector B.C., if we assume that the effective acceleration voltage V_E is twice of the first electron beam acceleration voltage V_A. That is, the following relation is found: From the analyzing magnetic field B_M where the negative current shows a peak, the curvature radius r of the mass analyzer and the effective acceleration voltage V_E, we can estimate the mass m of the negatively charged particle by,

$$m = \frac{Ze\,(B_M r)^2}{2V_E}$$

$$= \frac{8.8 \times 10^{-2}\, Z\,(B_M r)^2\, m_e}{V_E}, \quad \text{..... (1)}$$

where e is the electron charge, B_M is in gauss unit, r is in cm unit, V_E is in volt unit and m_e is the electron mass and Z is the charge number. For the curvature radius $r = 4.3$ cm of this mass analyzer, the Eq. (1) is rewritten by

$$m = \frac{1.63\, Z\, B_M^2}{V_E} m_e. \quad \text{..... (2)}$$

In the experiments as reported already,[1] we obtain $m = m_1 \approx 206\ m_e$ for the first peak of I^- and $m = m_2 \approx 290\ m_e$ for the second peak of I^-, assuming that $Z = 1$ and $V_E = 2\ V_A$.

3. New Experimental Research

A schematic diagram of the first experimental arrangement is shown in Fig. 5, where another negative current collector D.C. is added to measure a diffusional negative current in a back ground around the negative muonlike μ^- or pionlike π^- particle beam.

Dependences of a negative current I^- to the beam collector B.C. and another negative current I_D^- to the negative current collector D.C. on the analyzing magnetic field B_M are shown in Fig. 6 for various first electron beam acceleration voltage V_A. These experimental results agree with those of previous experiments.[1] That is, from Eq. (2), we can obtain $m = m_1 \approx 210\ m_e$ for each first peak of I^- and $m = m_2 \approx 290\ m_e$ for each second peak of I^-, assuming that $Z = 1$ and $V_E = 2\ V_A$. Besides, large peak values of the electron beam current I_e are shown near the small analyzing magnetic field B_M. (By a fringe effect of B_M, the exact relation of Eq. (2) is not obtained for the electron beam). In this experiment, the diffusional negative currents I_D^- are measured, where the area of negative current collector D.C. for I_D^- is about 10 cm^2 and that of the beam collector B.C. for I^- is about 0.25 cm^2. Thus, we can determine that each peak negative current density for the μ^- or π^- beam current of Fig. 6, is 26 $\mu A/cm^2$ (for peak of I^-) or 0.26 $\mu A/cm^2$ (for peak of I_D^-) in a case of the initial electron beam acceleration voltage $V_A = 400V$ and the collector bias voltage $V_S = 200V$. Then, we find that the diffusional negative current density j_D^- is about 1/100 of the beam collector current density j^-. That is, $j^- \gg j_D^-$. This fact shows that the negative muonlike or pionlike particle beam concentrates to the beam collector B.C. with the curvature of mass analyzer $r \approx 4.3$ cm.

A schematic diagram of the second experimental arrangement is shown in Fig. 7, where a metal plate (Cu) of about 1 cm in thickness is put behind the source X of negative muonlike or pionlike particle production in order to research characteristics of metal plate penetration of the μ^- or π^- beam. Dependences of a negative current I^- to the beam collector B.C. and another negative current I_D^- to the negative current collector D.C. on the analyzing magnetic field B_M are shown in Fig. 8. In comparison with the experimental results of Fig. 6, peaks of electron beam current I_e

near the weak analyzing magnetic field disappear while the other results are the same almost. From these experimental results, we may consider that the μ^- and π^- beam penetrate through the metal plate without energy loss. In the above experiment, positive ions of air (mainly N_2^+) are used. To investigate differences for the gas (air) and for the positive bias voltage V_S of the beam collector B.C. and the negative current collector D.C. with respect to the mass analyzer, an Ar gas is introduced in the plasma region (G) of Fig. 7. Then, dependences of I^- and I_D^- on B_M are shown for two bias voltages $V_S = 200V$ and $V_S = 100V$. We find that the experimental features do not vary in comparison to a case of air and do not depend on the positive bias voltage V_S.

A schematic diagram of the third experimental apparatus is shown in Fig. 10, where the magnetic mass analyzing region is surrounded by electrically floated metal plates (FMP), in order to be isolated from the μ^-, π^- source X and the secondary plasma S.P. (which is generated from a mixture of the injecting ion beam I.B. and the secondary electron beam S.E.B.). Moreover, the mass analyzing region is divided by a metal mesh (1.5 mm × 1.5 mm) region (1.5 cm × 3 cm) ME from the secondary plasma S.P. Thus, injections of electrons or positive ions from S.P. into the magnetic mass analyzing region are controlled by the mesh potential V_{ME} with respect to the mass analyzer. That is, for $V_E \geq 0$, the electrons of S.P. are much more injected and for $V_E < 0$, the positive ions of S.P. are much more injected into the mass analyzing region. At $V_E = -100V$, dependences of I^- to the beam collector B.C. and the positive ion current I_{ME}^+ to the metal mesh ME, on B_M are shown in Fig. 11. We find the similar experimental results (the two peaks of I^-) in comparison to those of Fig. 6 and 8. Next, at $V_E = 0$, dependences of I^- and the negative current I_{ME}^- to the ME, on B_M are shown in Fig. 12. Then, we find that the peak of I^- corresponding with the μ^- or π^- beam to the B.C., is much reduced. That is, the injection of positive ions into the mass analyzing region is a necessary condition to lead the μ^- or π^- beam to the B.C.

A dependence of the peak value I_P^- of the μ^- beam current I^- on the mesh potential V_{ME} are shown in Fig. 13. We find that the I_P^- increases for $V_{ME} < -50V$ with the positive ion current to the metal mesh ME. A back ground negative current I_{BA}^- near the B.C. is measured by a negative current collector as shown in Fig. 10. As a result, the negative current density of I_{BA} is below 1/10 of that of I_P^- in Fig. 11.

4. Discussion

The electron cyclotron radius r_{ce} is about 0.3 cm near the analyzing magnetic fields B_{MP} where the two peaks of I^- corresponding with the μ^- and π^- appear. Then, the positive ion cyclotron radius r_{ci} is about 60 cm for N_2^+ ions. Thus, for the mass analyzing radius $r \approx 4.3$ cm, an estimation is obtained by

$$r_{ce} \ll r \ll r_{ci}. \quad \cdots\cdots (3)$$

From this estimation, we consider at the $B_M = B_{MP}$ that electrons of the secondary plasma S.P. around the mass analyzing region can not enter it's region except the diffusional components, and that only the positive ions of S.P. can enter it's region and compensate the space charges of μ^- or π^- beam. Therefore, the space charges of μ^- or π^- beam in the previous experiments[1] and in the new experiments of Figs. 5 and 7, are compensated by the positive ions from S.P.

In the new experiment of Fig. 10, a compensation of the space charges for μ^- or π^- beam is controlled electrically by the mesh potential V_{ME}. Obviously, the peaks of I^- corresponding with μ^- or π^- beam to B.C., much increase for $V_{ME} < 0$ which determines injection of positive ions into the mass analyzing region. Inversely, the injection of positive ions is a necessary condition for μ^- or π^- beam to penetrate the metal plate without energy loss. Similarly, it is also a necessary condition to detect the μ^- or π^- beam on the beam collector B.C. at the analyzing position $r = 4.3$ cm.

These experimental results can not be explained from the ordinary penetration theories of charged particles (for electrons or ions). Because the μ^- or π^- beam energy is too low to penetrate the metal plate. As an explanation for the metal plate penetration, we consider the following reasons:

(1) Each Bohr radius of "negative muon or pion atom" at a ground state is much smaller ($\sim 10^{-2}$ Å) than that of "electron atom" (~1Å) because the negative muon or negative pion mass is much larger.

(2) The mean kinetic energies of the μ^- or π^- beam in these experiments are very low (200 eV ~ 1600 eV) in comparison with the ground state (bounded by nuclei) energy of negative muon

or negative pion atom $E_G = -3$ KeV ~ -5 KeV (which can be estimated to be 200 ~ 300 times larger that of "electron atom" $E_{GE} \approx -15$ eV).

Thus, the μ^- or π^- beam will be able to pass through the numerous intervals of metal nucleis in scales between ~1Å (electron Bohr radius) and ~10^{-2}Å (negative muon or pion Bohr radius). Then, in the space (the mass analyzing region) after the penetration of metal plate, the space charge effects of μ^- or π^- become important for a negative potential build-up due to the μ^- or π^- beam itself and a spatial spread of the μ^- or π^- beam. It should be noted that the space charge effects are more serious than those of electron beam as the mass of μ^- or π^- is much larger than that of electron. Therefore, some positive ions must be supplied into the space (the mass analyzing region) after the penetration in order to compensate the negative space charge. For the metal mesh (ME of Fig. 10) potential $V_E < 0$, the positive ions in the analyzing region are certainly detected when the floating metal plate (FMP of Fig. 10) is connected to a power supply which is electrically negative with respect to the mass analyzer.

Reference

1. J. Uramoto, *NIFS Report* No. 277 (1994).

Fig. 1 and Fig. 2: Schematic diagrams of the basic experimental apparatus.

F: Filament as electron emitter. K: Cathode of electron gun. A: Anode of electron gun. V_A: Initial electron acceleration voltage. I_A: Total negative current. F.E.B.: First electron beam. G: Neutral gas. D: Decelerator of F.E.B. S: Entrance slit (3 mm × 10 mm). Ins: Insulator. I.B.: Ion beam. S.E.B.: Second electron beam. e: Electrons with cyclotron motions. μ^-: Negative muonlike particle. (M.A.): Mass analyzer. Fe: Iron. C: Magnetic Coil. (N): North pole of electro-magnet. (S): South pole. B_M: Analyzing magnetic field. B.C.: Beam collector. I^-: Negative current to B.C. V_S: Bias voltage of B.C. with respect to mass analyzer body. S.P.: Secondary plasma generating outside the mass analyzing region. X: Entrance of uniform magnetic field. i: Ion bunch. π^-: Negative pionlike particle. The neutral gas (air) pressure is about 3×10^{-6} Torr in the electron gun region and 1×10^{-5} Torr in the plasma region (F.E.B. and G in Fig. 2). The total anode current (of electron gun) I_A is kept to the $I_A = 2.5$ mA while the anode (electron gun) voltage V_A is varied. A bias voltage V_S for the beam collector B.C. and the diffusional current collector D.C. is usually kept to $V_S = 200$V.

Fig. 3 Fringe magnetic field distribution.

B_M: Analyzing magnetic field of (M.A.). B_O: Uniform magnetic field inside (M.A.). X: End of uniform magnetic field. S: Entrance slit position. Fe: Magnetic field distribution in a case using iron plate as D in Fig. 1. Cu: Magnetic field distribution in a case using copper plate as D in Fig. 1.

Fig. 4 Applied electrical potential distribution.

V: Electrical potential. V_A: Initial potential (voltage) of electron gun anode. V_E: Effective potential for μ^- (negative muonlike particle) and π^- (negative pionlike particle). e_0: Initial electrons from electron gun cathode. e_1: First electron beam. e_2: Second electron beam. i_1: Positive ion beam from plasma. i_2: Second positive ion beam. e–B: Electron bunch due to magnetic cyclotron motion. i–B: Positive ion bunch due to electrical retardation. K: Cathode position of electron gun. A: Anode position of electron gun. S: Slit position of mass analyzer. X: Entrance position of analyzing uniform magnetic field. $+V_A$: Additional potential generated by stopping the positive ion beam.

Fig. 5 A schematic diagram of the first experimental arrangement.

D.C.: Diffusional negative current collector. I_D^-: Negative current to D.C.. Others: (see Fig. 1 and Fig. 2 captions).

Fig. 6 Dependences of a negative current I^- to the beam collector B.C. and another negative current I_D^- to the negative current collector D.C. on the analyzing magnetic field B_M.

I_e: Electron current. I_e (400V): I_e characteristic at the initial electron beam acceleration voltage $V_A = 400V$. I^- (200V): I^- characteristic at $V_A = 200V$. I^- (400V): I^- characteristic at $V_A = 400V$. I^- (800V): I^- characteristic at $V_A = 800V$. I_D^- (400V): I_D^- characteristic at $V_A = 400V$.

Fig. 7 A schematic diagram of the second experimental arrangement (for metal plate penetration).

MP: Metal (Cu) plate of about 1 cm in thickness. Others: (see Fig. 1, Fig. 2 and Fig. 5 captions).

Fig. 8 Dependences of a negative current I^- to the beam collector B.C. and another negative current I_D^- to the negative current collector D.C. on the analyzing magnetic field B_M (under metal plate penetration).

I^- (200V): I^- characteristic at the initial electron beam acceleration voltage $V_A = 200V$. I^- (400V): I^- characteristic at $V_A = 400V$. I^- (800V): I^- characteristic at $V_A = 800V$. I_D^- (400V): I_D^- characteristic at $V_A = 400V$.

Fig. 9 Dependences of I^- and I_D^- on B_M for Ar gas plasma and the positive bias voltage V_S of B.C. and D.C., $V_S = 200V$ or $V_S = 100V$. The Ar gas pressure is about 1.5×10^{-5} Torr in the electron gun region and 1×10^{-4} Torr in the plasma region (F.E.B. and G in Fig. 2).

Fig. 10 A schematic diagram of the third experimental arrangement.

ME: Metal mesh (1.5 mm × 1.5 mm) of (1.5 cm × 3 cm) in area. V_{ME}: Potential of ME. I_{ME}: Current to ME. FMP: Floating metal plate. I_{BA}^- Negative current to back ground collector near B.C. ION: Positive ion current from the secondary plasma S.P.

Fig. 11 Dependences of I^- (to B.C.) and I^+_{ME} (positive ion current to ME) on B_M under metal mesh potential $V_E = -100V$.

I^-_P: Peak value of I^-. I^+_{MEP}: Peak value of I^+_{ME}.

Fig. 12 Dependences of I^- (to B.C.) and I^-_{ME} (negative current to ME) on B_M under metal mesh potential $V_E = 0$.

I^-_P: Peak value of I^-. I^-_{MEP}: Peak value of I^-_{ME}.

Fig. 13 Dependence of peak value I^-_P of I^- on the metal mesh potential V_{ME} and dependence of peak value (I^+_{MEP} or I^-_{MEP}) of metal mesh current I_{ME} on V_{ME}.

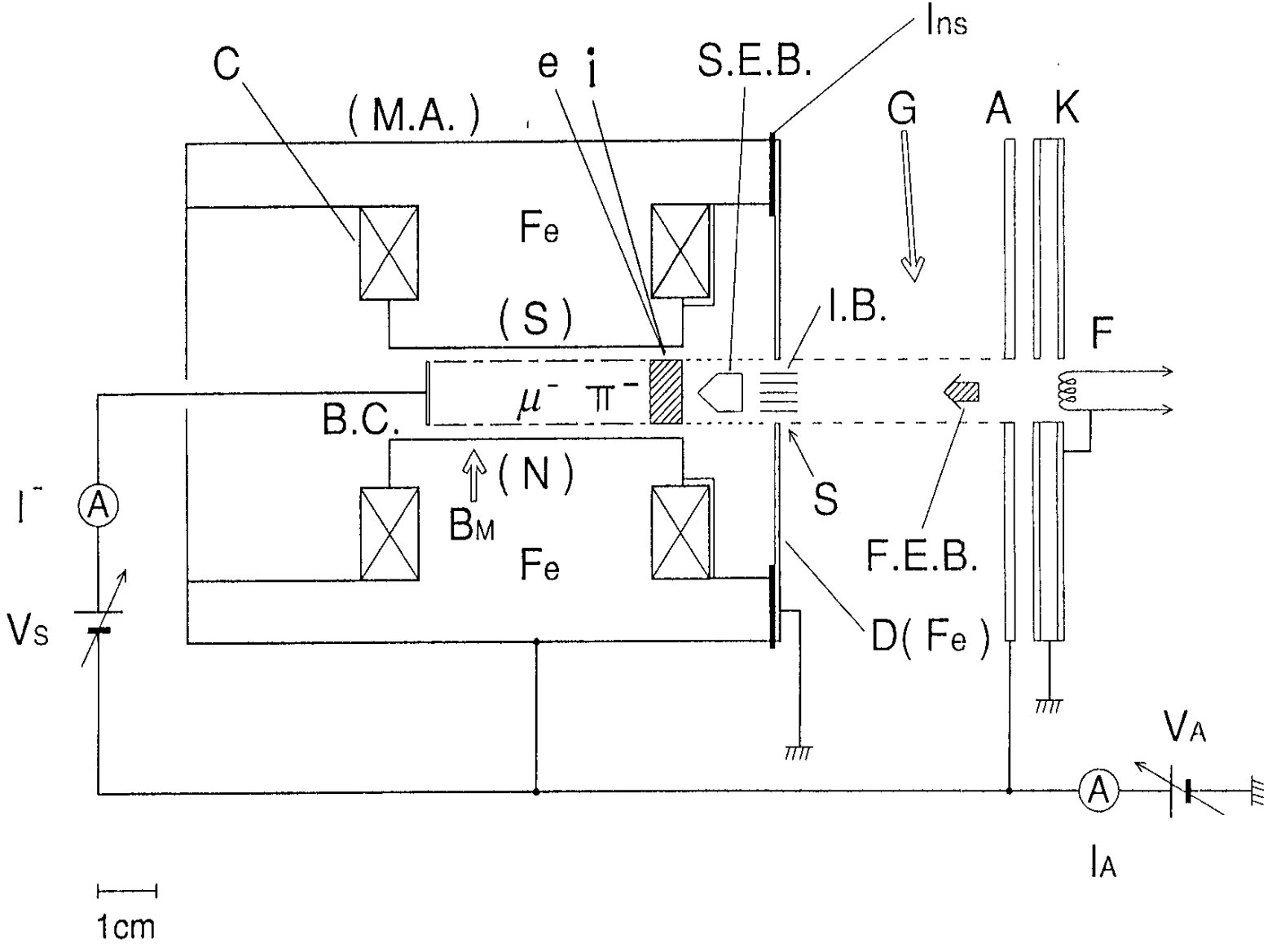

Fig. 1

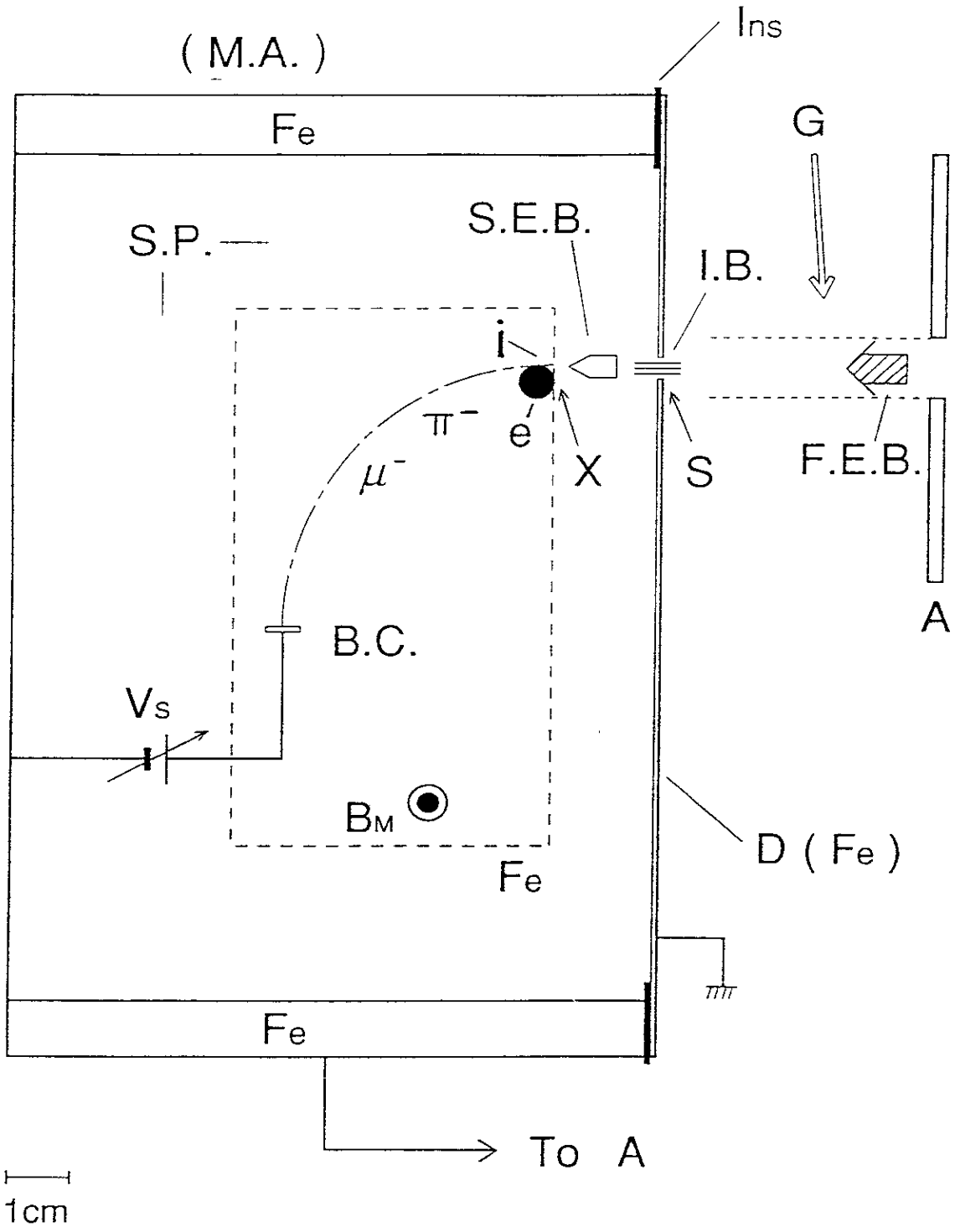

Fig. 2

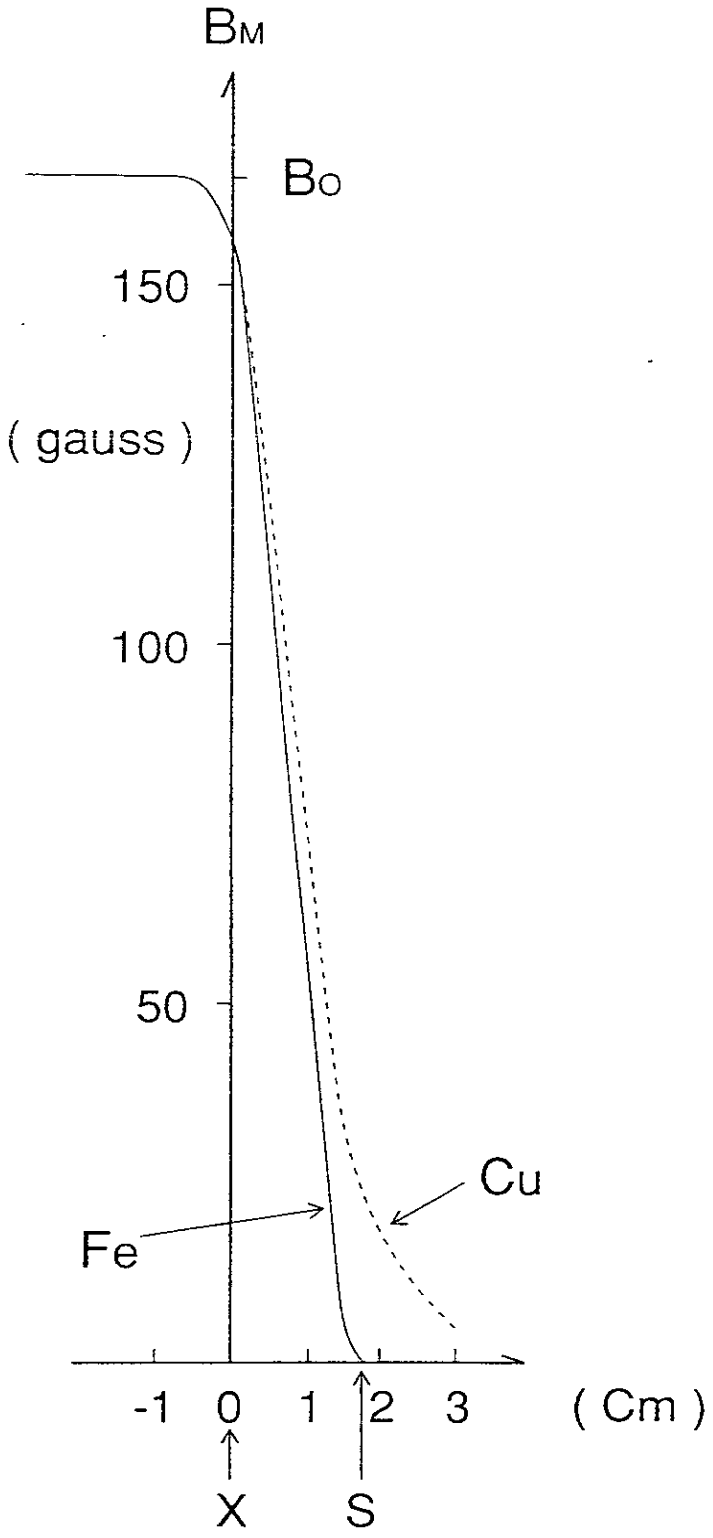

Fig. 3

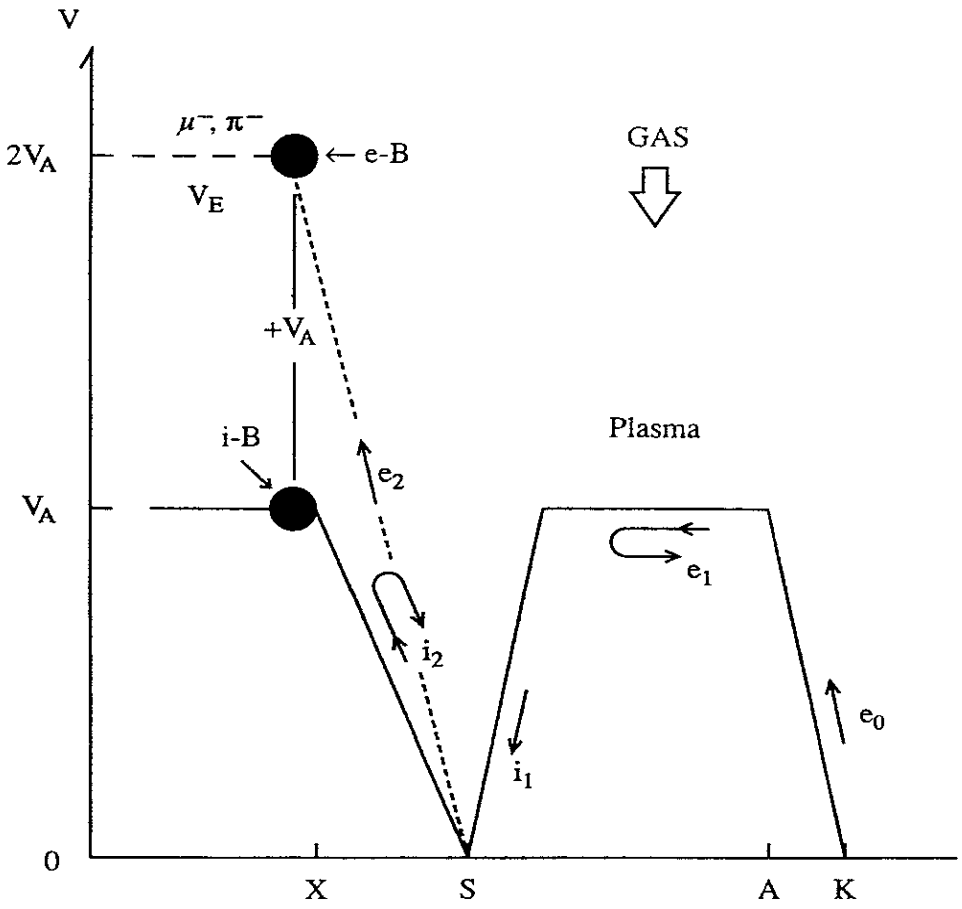

Fig. 4

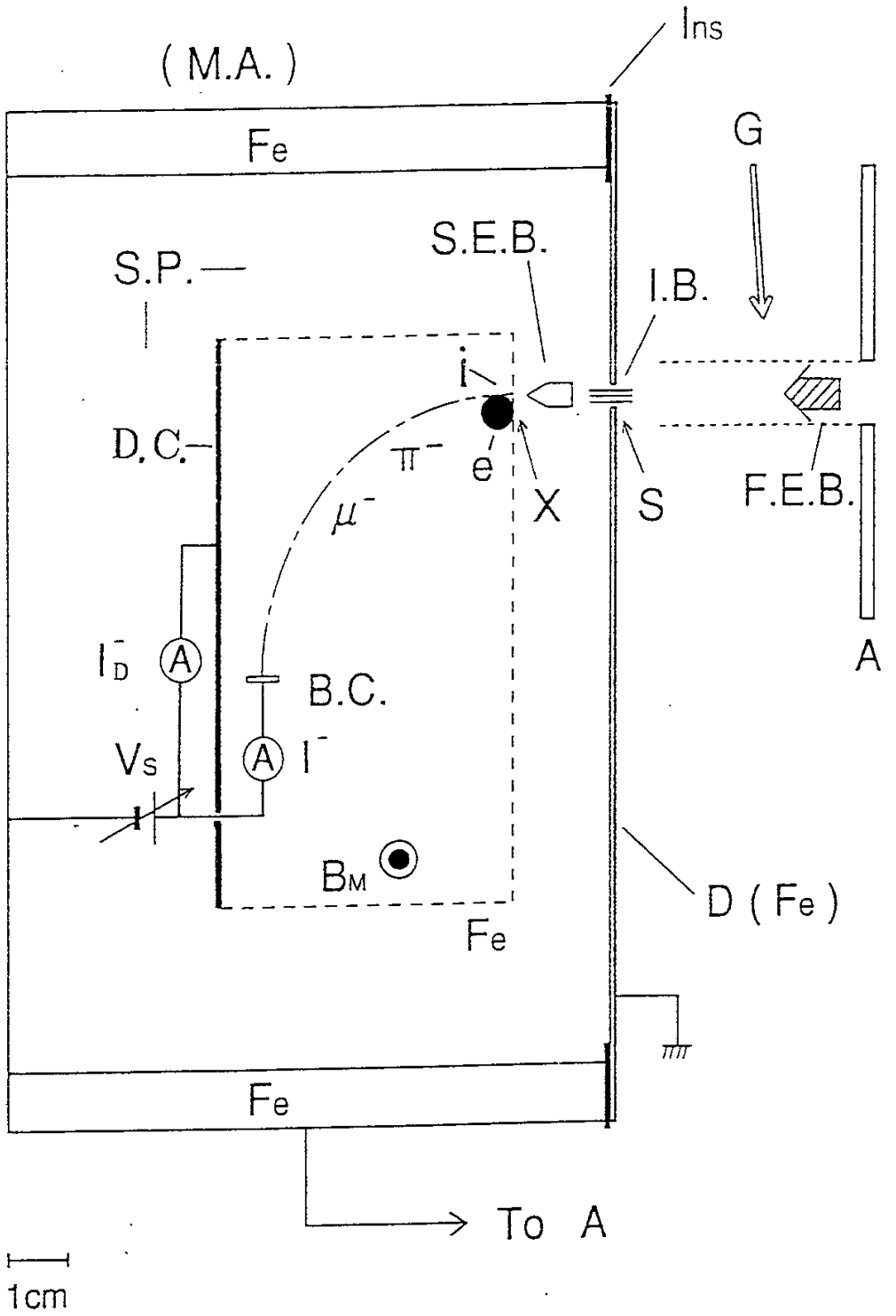
(M.A.)
Ins
Fe
G
S.E.B.
S.P.
I.B.
i
D.C.
π⁻
e
μ⁻
X
S
F.E.B.
A
I⁻D
A
B.C.
Vs
A
I⁻
BM
D (Fe)
Fe
Fe
To A
1cm

Fig. 5

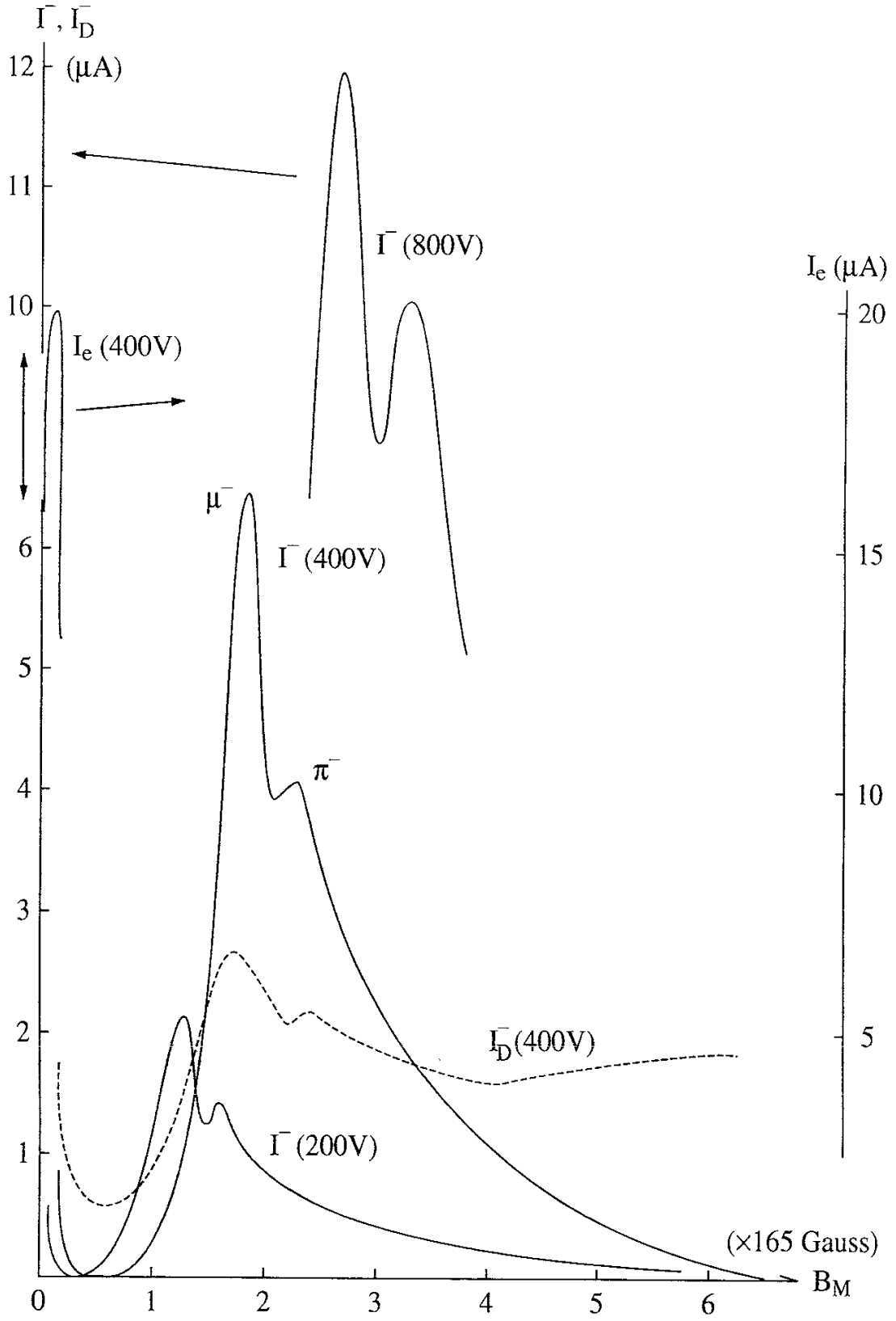
I⁻, I⁻D
(μA)
12
11
10
6
5
4
3
2
1
0
1
2
3
4
5
6
I⁻ (800V)
Ie (400V)
μ⁻
I⁻ (400V)
π⁻
I⁻D (400V)
I⁻ (200V)
Ie (μA)
20
15
10
5
(×165 Gauss)
BM

Fig. 6

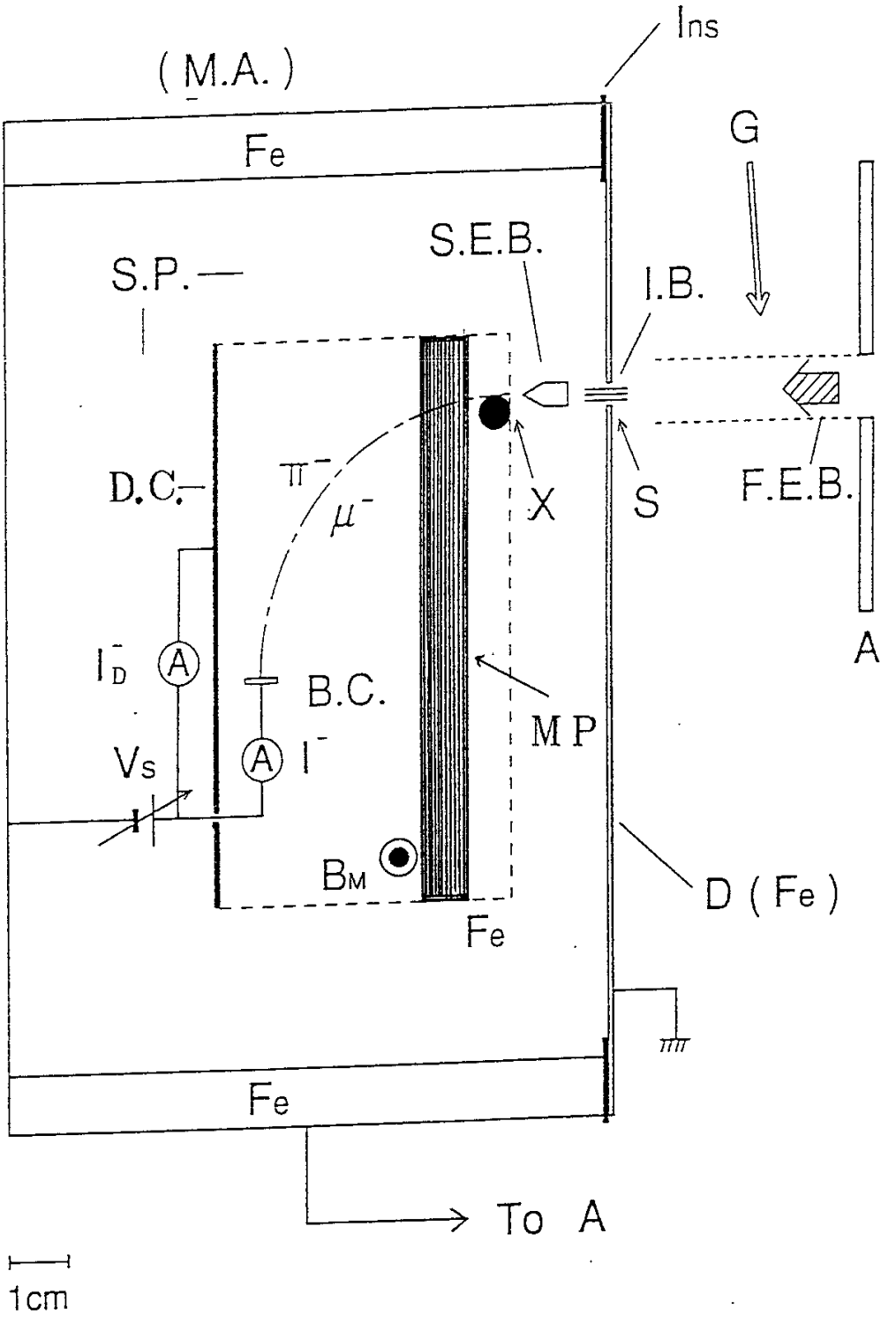
Ins
(M.A.)
Fe
G
S.E.B.
S.P.
I.B.
D.C.
π⁻
μ⁻
X
S
F.E.B.
A
I⁻D
A
B.C.
MP
Vs
A
I⁻
BM
Fe
D (Fe)
Fe
To A
1cm

Fig. 7

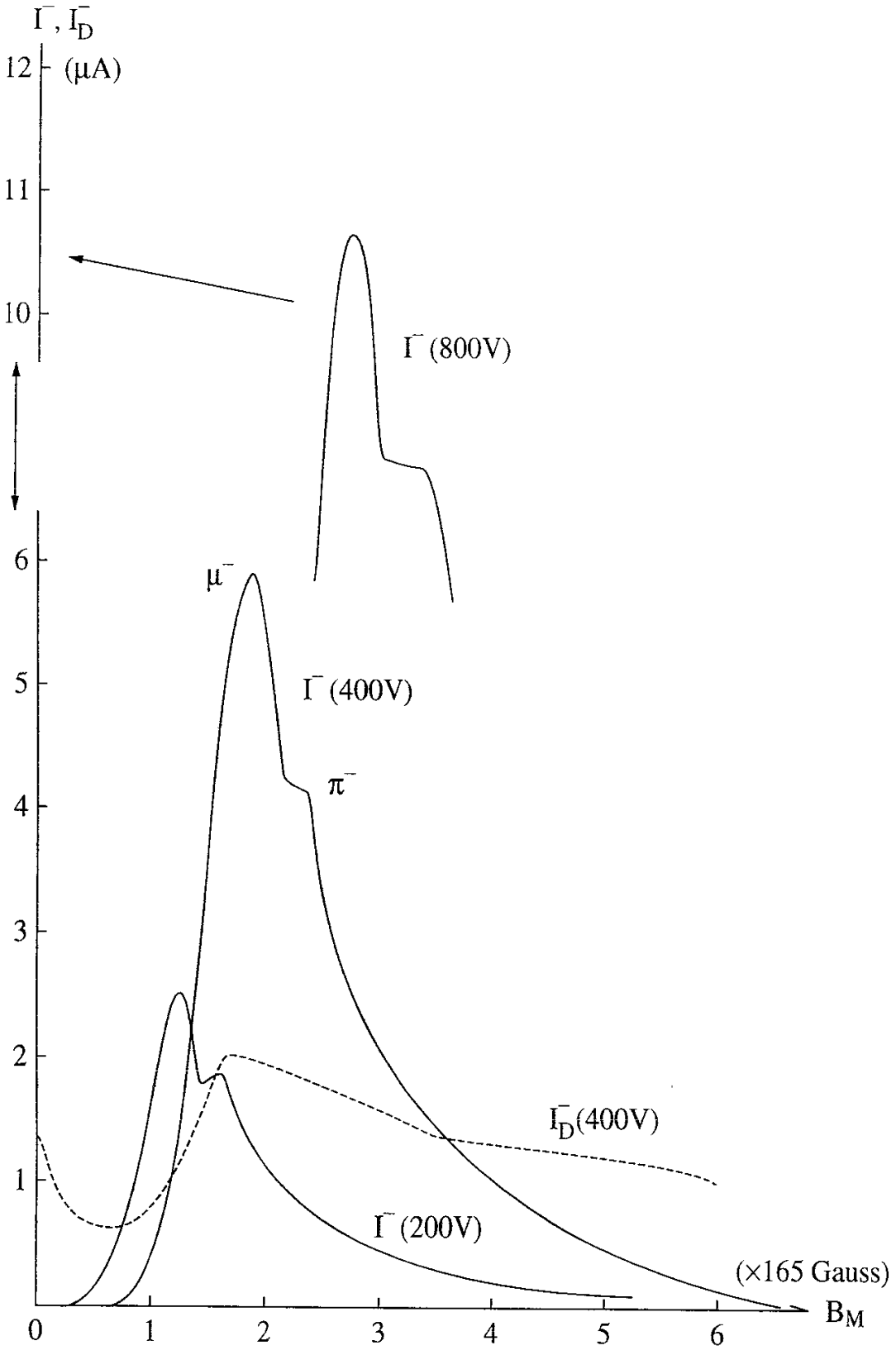
I⁻, I⁻D
12
(μA)
11
10
I⁻ (800V)
6
μ⁻
5
I⁻ (400V)
π⁻
4
3
2
I⁻D(400V)
1
I⁻ (200V)
(×165 Gauss)
0
1
2
3
4
5
6
BM

Fig. 8

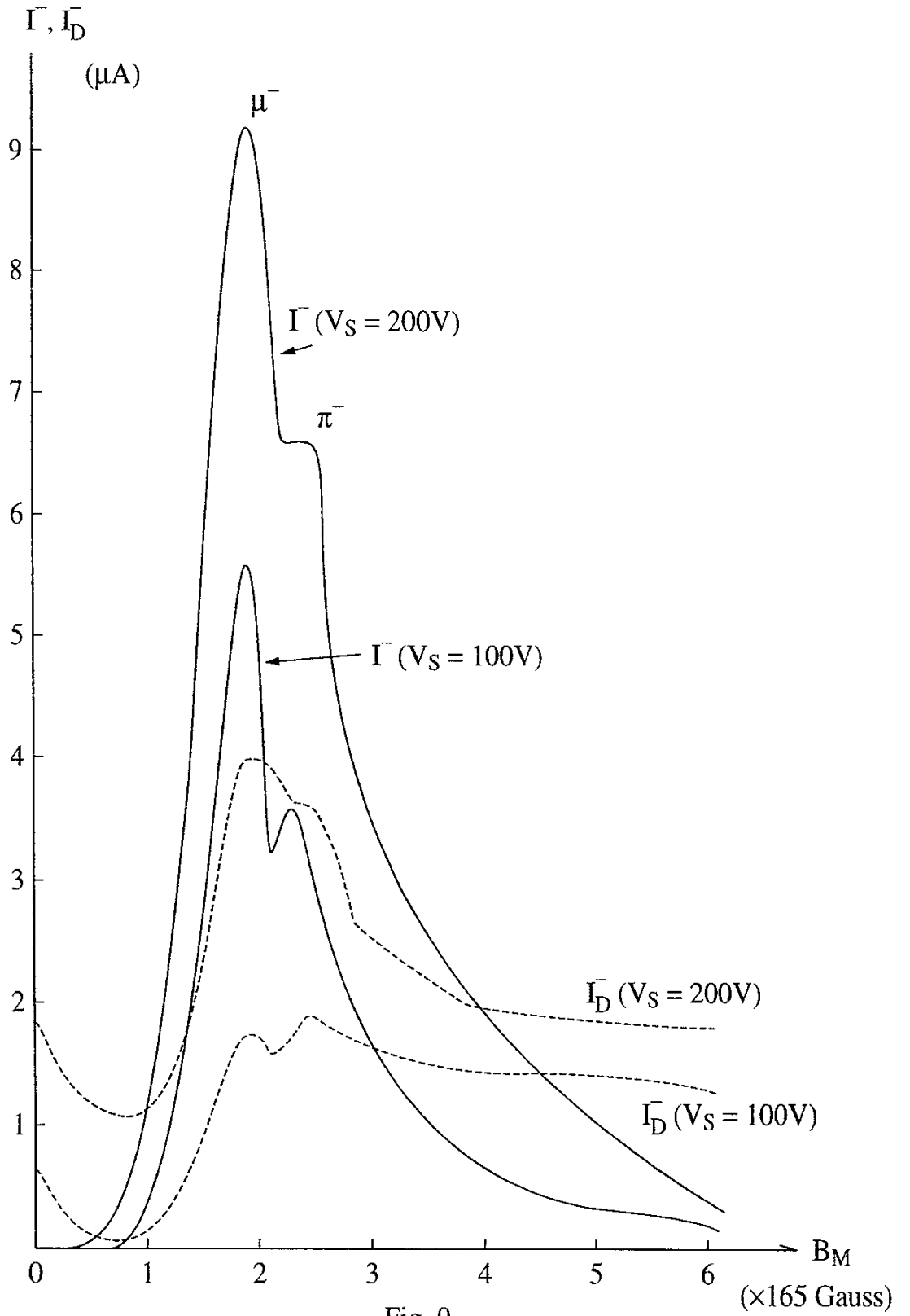
I⁻, I⁻D
(μA)
μ⁻
9
8
I⁻ (VS = 200V)
7
π⁻
6
5
I⁻ (VS = 100V)
4
3
2
I⁻D (VS = 200V)
1
I⁻D (VS = 100V)
BM
0
1
2
3
4
5
6
(×165 Gauss)

Fig. 9

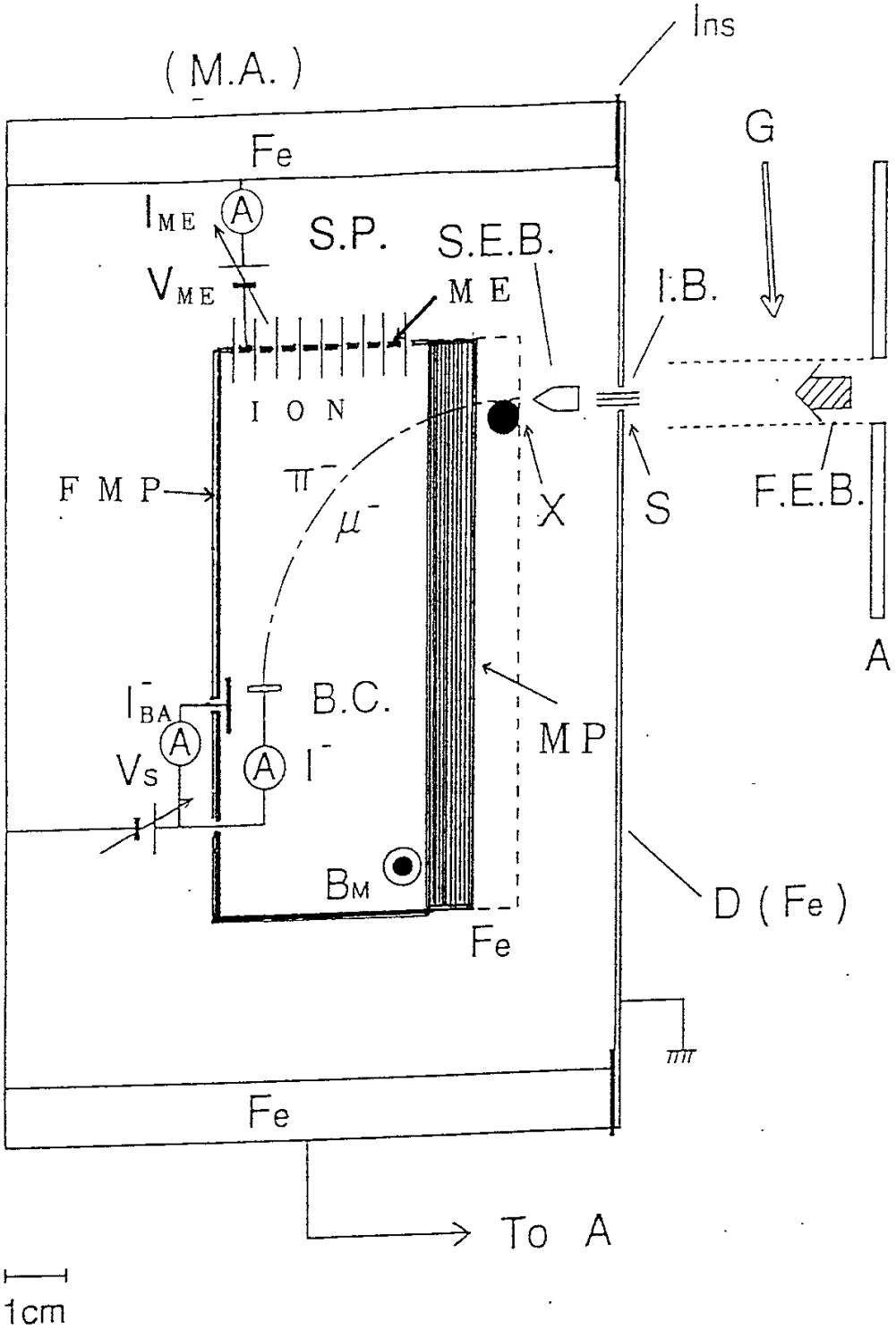
Ins
(M.A.)
Fe
G
I_{ME}
A
S.P.
S.E.B.
V_{ME}
ME
I.B.
ION
FMP
π^-
μ^-
X
S
F.E.B.
A
I^-_{BA}
B.C.
MP
Vs
A
I^-
B_M
D (Fe)
Fe
Fe
To A
1cm

Fig.10

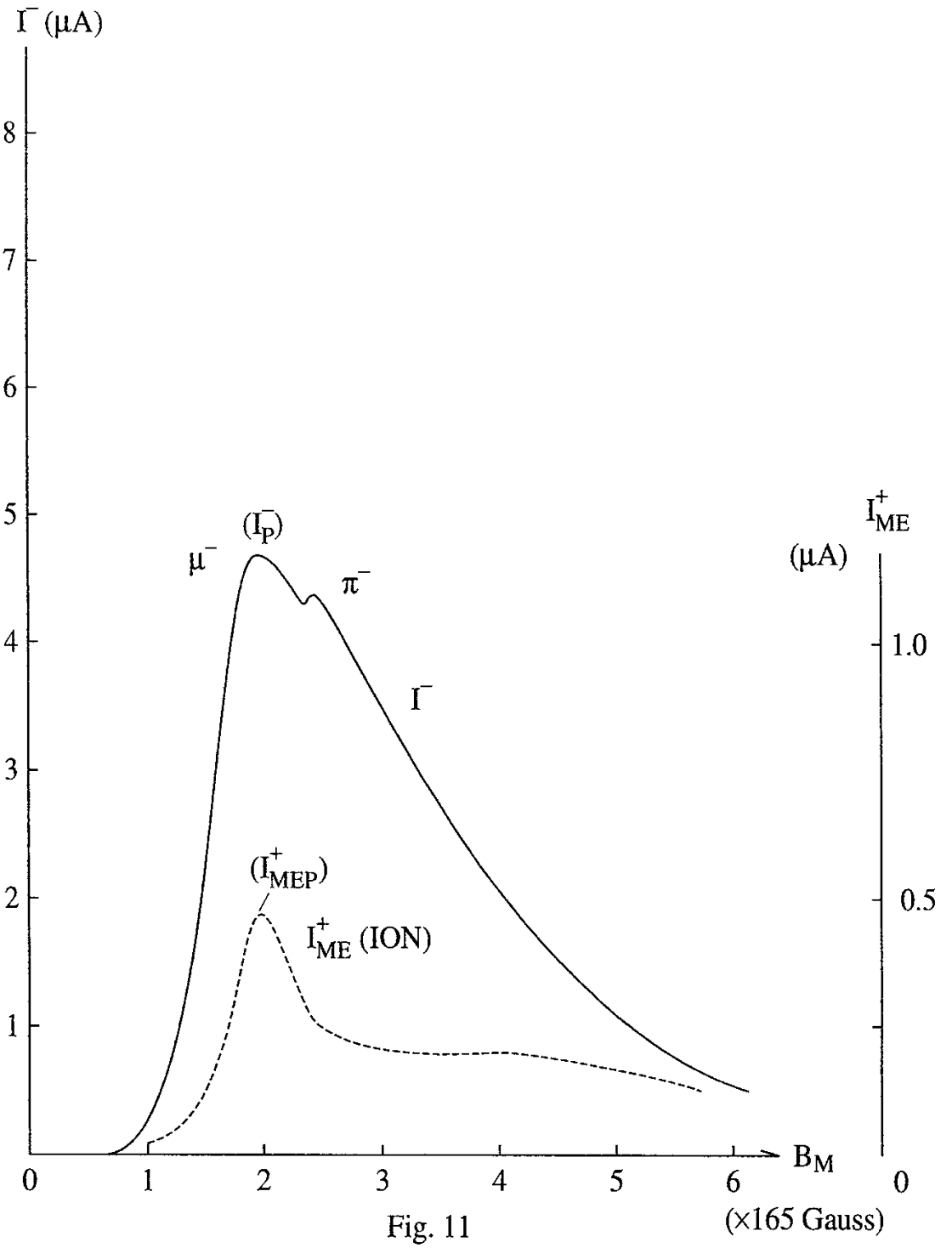
I⁻ (μA)
8
7
6
5
4
3
2
1
0
1
2
3
4
5
6
B_M
(×165 Gauss)
μ⁻
(I_P⁻)
π⁻
I⁻
(I⁺_MEP)
I⁺_ME (ION)
I⁺_ME
(μA)
1.0
0.5
0

Fig. 11

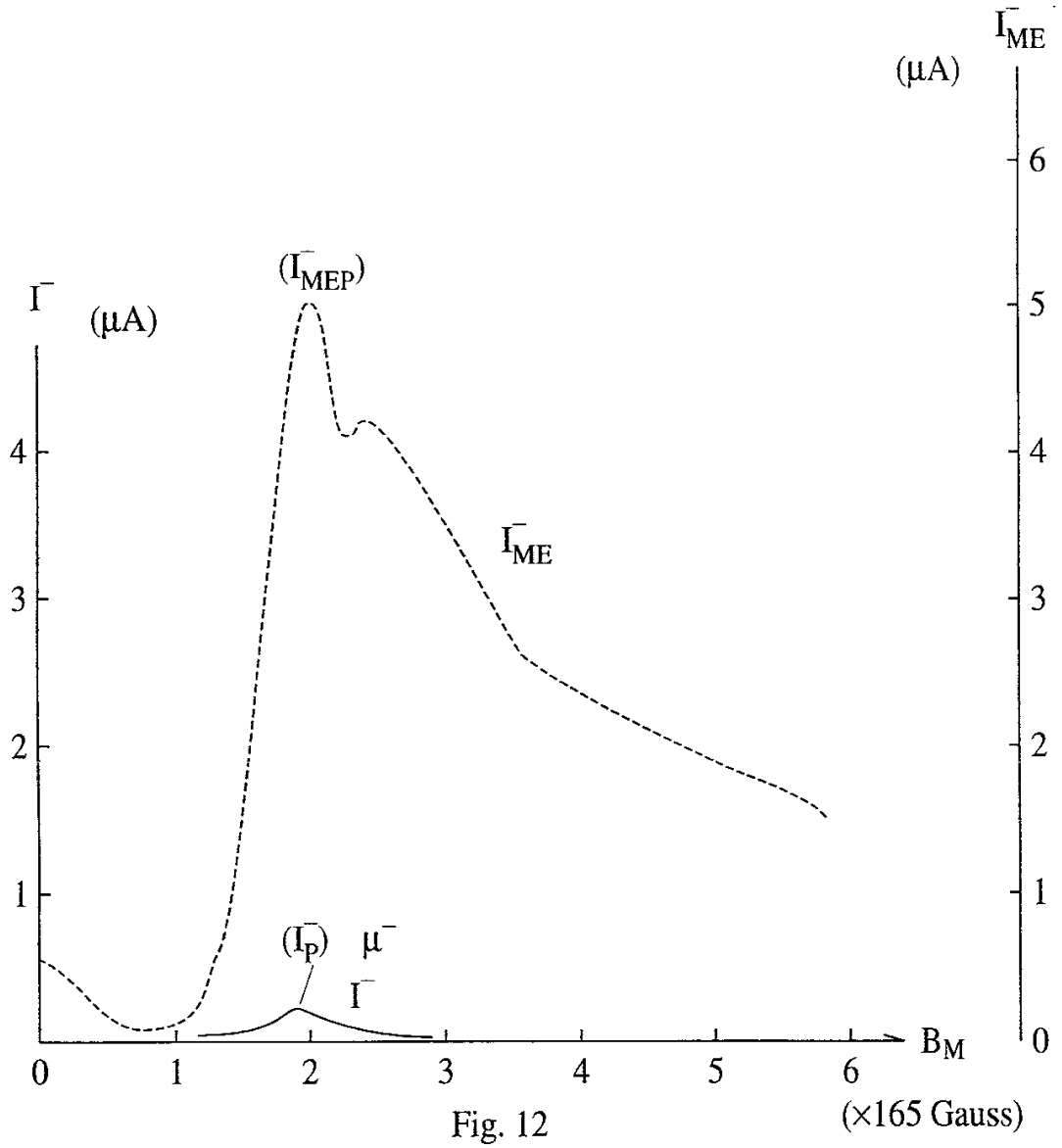

Fig. 12

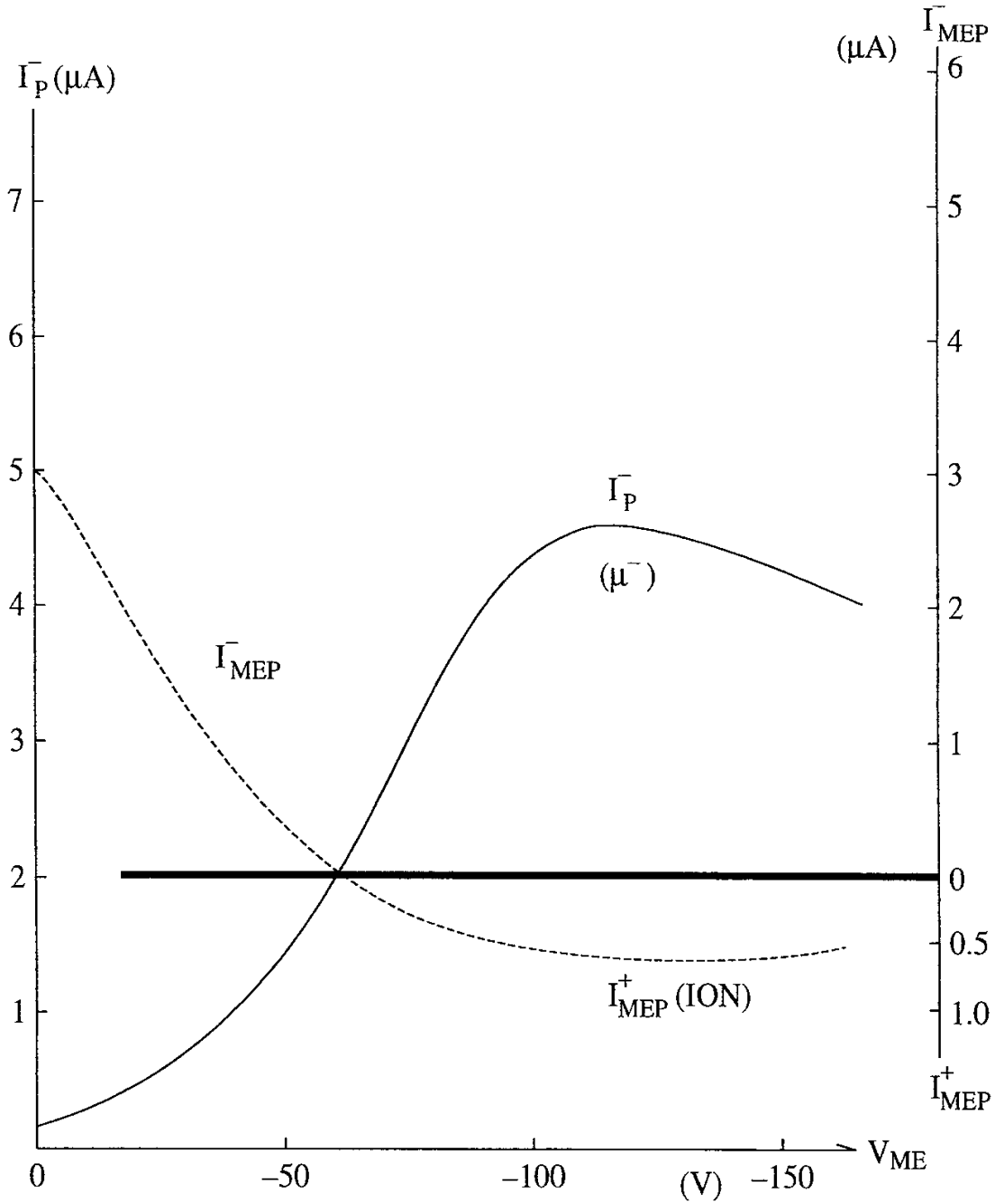
I^-_P (μA)
I^-_{MEP} (μA)
7
6
5
4
3
2
1
6
5
4
3
2
1
0
0.5
1.0
I^-_P
(μ^-)
I^-_{MEP}
I^+_{MEP} (ION)
I^+_{MEP}
V_{ME}
0
−50
−100
(V)
−150

Fig. 13

Recent Issues of NIFS Series

NIFS-304 K. Ida, H. Idei, H. Sanuki, K. Itoh, J. Xu, S. Hidekuma, K. Kondo, A. Sahara, H. Zushi, S.-I. Itoh, A. Fukuyama, K. Adati, R. Akiyama, S. Bessho, A. Ejiri, A. Fujisawa, M. Fujiwara, Y. Hamada, S. Hirokura, H. Iguchi, O. Kaneko, K. Kawahata, Y. Kawasumi, M. Kojima, S. Kubo, H. Kuramoto, A. Lazaros, R. Liang, K. Matsuoka, T. Minami, T. Mizuuchi, T. Morisaki, S. Morita, K. Nagasaki, K. Narihara, K. Nishimura, A. Nishizawa, T. Obiki, H. Okada, S. Okamura, T. Ozaki, S. Sakakibara, H. Sakakita, A. Sagara, F. Sano, M. Sasao, K. Sato, K.N. Sato, T. Saeki, S. Sudo, C. Takahashi, K. Tanaka, K. Tsumori, H.Yamada, I. Yamada, Y. Takita, T. Tuzuki, K. Toi and T. Watari, *Control of Radial Electric Field in Torus Plasma;* Sep. 1994 (IAEA-CN-60/A-2-IV-2)

NIFS-305 T. Hayashi, T. Sato, N. Nakajima, K. Ichiguchi, P. Merkel, J. Nührenberg, U. Schwenn, H. Gardner, A. Bhattacharjee and C.C.Hegna, *Behavior of Magnetic Islands in 3D MHD Equilibria of Helical Devices*; Sep. 1994 (IAEA-CN-60/D-2-II-4)

NIFS-306 S. Murakami, M. Okamoto, N. Nakajima, K.Y. Watanabe, T. Watari, T. Mutoh, R. Kumazawa and T. Seki, *Monte Carlo Simulation for ICRF Heating in Heliotron/Torsatrons*; Sep. 1994 (IAEA-CN-60/D-P-I-14)

NIFS-307 Y. Takeiri, A. Ando, O. Kaneko, Y. Oka, K. Tsumori, R. Akiyama, E. Asano, T. Kawamoto, T. Kuroda, M. Tanaka and H. Kawakami, *Development of an Intense Negative Hydrogen Ion Source with a Wide-Range of External Magnetic Filter Field*; Sep. 1994

NIFS-308 T. Hayashi, T. Sato, H.J. Gardner and J.D. Meiss, *Evolution of Magnetic Islands in a Heliac*; Sep. 1994

NIFS-309 H. Amo, T. Sato and A. Kageyama, *Intermittent Energy Bursts and Recurrent Topological Change of a Twisting Magnetic Flux Tube*; Sep.1994

NIFS-310 T. Yamagishi and H. Sanuki, *Effect of Anomalous Plasma Transport on Radial Electric Field in Torsatron/Heliotron*; Sep. 1994

NIFS-311 K. Watanabe, T. Sato and Y. Nakayama, *Current-profile Flattening and Hot Core Shift due to the Nonlinear Development of Resistive Kink Mode*; Oct. 1994

NIFS-312 M. Salimullah, B. Dasgupta, K. Watanabe and T. Sato,
Modification and Damping of Alfvén Waves in a Magnetized Dusty Plasma; Oct. 1994

NIFS-313 K. Ida, Y. Miura, S -I. Itoh, J.V. Hofmann, A. Fukuyama, S. Hidekuma, H. Sanuki, H. Idei, H. Yamada, H. Iguchi, K. Itoh,
Physical Mechanism Determining the Radial Electric Field and its Radial Structure in a Toroidal Plasma; Oct. 1994

NIFS-314 Shao-ping Zhu, R. Horiuchi, T. Sato and The Complexity Simulation Group,
Non-Taylor Magnetohydrodynamic Self-Organization; Oct. 1994

NIFS-315 M. Tanaka,
Collisionless Magnetic Reconnection Associated with Coalescence of Flux Bundles; Nov. 1994

NIFS-316 M. Tanaka,
Macro-EM Particle Simulation Method and A Study of Collisionless Magnetic Reconnection; Nov. 1994

NIFS-317 A. Fujisawa, H. Iguchi, M. Sasao and Y. Hamada,
Second Order Focusing Property of 210° Cylindrical Energy Analyzer; Nov. 1994

NIFS-318 T. Sato and Complexity Simulation Group,
Complexity in Plasma - A Grand View of Self- Organization; Nov. 1994

NIFS-319 Y. Todo, T. Sato, K. Watanabe, T.H. Watanabe and R. Horiuchi,
MHD-Vlasov Simulation of the Toroidal Alfvén Eigenmode; Nov. 1994

NIFS-320 A. Kageyama, T. Sato and The Complexity Simulation Group,
Computer Simulation of a Magnetohydrodynamic Dynamo II: Nov. 1994

NIFS-321 A. Bhattacharjee, T. Hayashi, C.C.Hegna, N. Nakajima and T. Sato,
Theory of Pressure-induced Islands and Self-healing in Three-dimensional Toroidal Magnetohydrodynamic Equilibria; Nov. 1994

NIFS-322 A. Iiyoshi, K. Yamazaki and the LHD Group,
Recent Studies of the Large Helical Device: Nov. 1994

NIFS-323 A. Iiyoshi and K. Yamazaki,
The Next Large Helical Devices; Nov. 1994

NIFS-324 V.D. Pustovitov
Quasisymmetry Equations for Conventional Stellarators; Nov. 1994

NIFS-325 A. Taniike, M. Sasao, Y. Hamada, J. Fujita, M. Wada,
The Energy Broadening Resulting from Electron Stripping Process of a Low Energy Au^- Beam; Dec. 1994

NIFS-326 I. Viniar and S. Sudo,
New Pellet Production and Acceleration Technologies for High Speed Pellet Injection System "HIPEL" in Large Helical Device; Dec. 1994

NIFS-327 Y. Hamada, A. Nishizawa, Y. Kawasumi, K. Kawahata, K. Itoh, A. Ejiri, K. Toi, K. Narihara, K. Sato, T. Seki, H. Iguchi, A. Fujisawa, K. Adachi, S. Hidekuma, S. Hirokura, K. Ida, M. Kojima, J. Koong, R. Kumazawa, H. Kuramoto, R. Liang, T. Minami, H. Sakakita, M. Sasao, K.N. Sato, T. Tsuzuki, J. Xu, I. Yamada, T. Watari,
Fast Potential Change in Sawteeth in JIPP T-IIU Tokamak Plasmas; Dec. 1994

NIFS-328 V.D. Pustovitov,
Effect of Satellite Helical Harmonics on the Stellarator Configuration; Dec. 1994

NIFS-329 K. Itoh, S-I. Itoh and A. Fukuyama,
A Model of Sawtooth Based on the Transport Catastrophe; Dec. 1994

NIFS-330 K. Nagasaki, A. Ejiri,
Launching Conditions for Electron Cyclotron Heating in a Sheared Magnetic Field; Jan. 1995

NIFS-331 T.H. Watanabe, Y. Todo, R. Horiuchi, K. Watanabe, T. Sato,
An Advanced Electrostatic Particle Simulation Algorithm for Implicit Time Integration; Jan. 1995

NIFS-332 N. Bekki and T. Karakisawa,
Bifurcations from Periodic Solution in a Simplified Model of Two-dimensional Magnetoconvection; Jan. 1995

NIFS-333 K. Itoh, S.-I. Itoh, M. Yagi, A. Fukuyama,
Theory of Anomalous Transport in Reverse Field Pinch; Jan. 1995

NIFS-334 K. Nagasaki, A. Isayama and A. Ejiri
Application of Grating Polarizer to 106.4GHz ECH System on Heliotron-E; Jan. 1995

NIFS-335 H. Takamaru, T. Sato, R. Horiuchi, K. Watanabe and Complexity Simulation Group,
A Self-Consistent Open Boundary Model for Particle Simulation in Plasmas; Feb. 1995

NIFS-336 B.B. Kadomtsev,
Quantum Telegragh : is it possible?; Feb. 1995

NIFS-337 B.B.Kadomtsev,
Ball Lightning as Self-Organization Phenomenon; Feb. 1995

NIFS-338 Y. Takeiri, A. Ando, O. Kaneko, Y. Oka, K. Tsumori, R. Akiyama, E. Asano, T. Kawamoto, M. Tanaka and T. Kuroda,
High-Energy Acceleration of an Intense Negative Ion Beam; Feb. 1995

NIFS-339 K. Toi, T. Morisaki, S. Sakakibara, S. Ohdachi, T.Minami, S. Morita, H. Yamada, K. Tanaka, K. Ida, S. Okamura, A. Ejiri, H. Iguchi, K. Nishimura, K. Matsuoka. A. Ando, J. Xu, I. Yamada, K. Narihara, R. Akiyama, H. Idei, S. Kubo, T. Ozaki, C. Takahashi, K. Tsumori,
H-Mode Study in CHS; Feb. 1995

NIFS-340 T. Okada and H. Tazawa,
Filamentation Instability in a Light Ion Beam-plasma System with External Magnetic Field; Feb. 1995

NIFS-341 T. Watanbe, G. Gnudi,
A New Algorithm for Differential-Algebraic Equations Based on HIDM; Feb. 13, 1995

NIFS-342 Y. Nejoh,
New Stationary Solutions of the Nonlinear Drift Wave Equation; Feb. 1995

NIFS-343 A. Ejiri, S. Sakakibara and K. Kawahata,
Signal Based Mixing Analysis for the Magnetohydrodynamic Mode Reconstruction from Homodyne Microwave Reflectometry; Mar.. 1995

NIFS-344 B.B.Kadomtsev, K. Itoh, S.-I. Itoh
Fast Change in Core Transport after L-H Transition; Mar. 1995

NIFS-345 W.X. Wang, M. Okamoto, N. Nakajima and S. Murakami,
An Accurate Nonlinear Monte Carlo Collision Operator; Mar. 1995

NIFS-346 S. Sasaki, S. Takamura, S. Masuzaki, S. Watanabe, T. Kato, K. Kadota,
Helium I Line Intensity Ratios in a Plasma for the Diagnostics of Fusion Edge Plasmas; Mar. 1995

NIFS-347 M. Osakabe,
Measurement of Neutron Energy on D-T Fusion Plasma Experiments; Apr. 1995

NIFS-348 M. Sita Janaki, M.R. Gupta and Brahmananda Dasgupta,
Adiabatic Electron Acceleration in a Cnoidal Wave; Apr. 1995

NIFS-349 J. Xu, K. Ida and J. Fujita,
A Note for Pitch Angle Measurement of Magnetic Field in a Toroidal Plasma Using Motional Stark Effect; Apr. 1995